# Supporting Information

## Czub and Grubmüller 10.1073/pnas.1018686108

### SI Text

**Central Shaft Elasticity: Analysis of Statistical Error.** To assess the statistical significance of the agreement between our molecular dynamics (MD)-derived and the measured values of torsional moduli, we employed a Brownian dynamics (BD)-based procedure. First, based on MD data (Fig. 2*A*), we calculated time autocorrelation functions for the angle of rotation of the considered γ-segment around the global axis for the CL1 and CL2 mutants (Fig. S2). By fitting the double exponential model to the obtained curves we identified two contributions to the overall decay, a fast component, with the relaxation time $\tau$ of $200 \pm 20$ ps, attributed to fast structural rearrangements within the considered segment, and a slow component, with relaxation time of $6.8 \pm 1.9$ and $2.3 \pm 0.22 \times 10^3$ ps for the CL1 and CL2 mutants, respectively, corresponding to the rotary motion around the global axis. Accordingly, in addition to the convergence of the torsional moduli obtained for the original MD data, Fig. 2*B* shows the curves with the fast component of the angular fluctuations filtered out (in red).

From the relaxation times, we estimated the diffusion constants for the rotary motion of the γ-segment to be $4.0 \pm 1.0$ and $2 \pm 0.3 \times 10^{-3}$ deg$^2$/ps for CL1 and CL2, respectively. These values were subsequently used to perform, for each protein, 20,000 separate 100-ns-long Brownian dynamics (Langevin dynamics in the overdamped limit) simulations of diffusive motion in a one-dimensional harmonic potential, using experimental values of the torsional modulus as the curvature. The initial angular positions for these simulations were randomly chosen from the corresponding equilibrium distribution. Afterwards, for each four independent 100-ns BD simulations, the same averaging scheme for calculating the torsional moduli was employed as before for the MD data. The distributions of the BD-derived torsional moduli are shown in orange in Fig. 2*C*, together with 10 exemplary curves showing the convergence of the torsional modulus value with increasing length of the trajectory taken for analysis. As can be seen, for both the CL1 and CL2 mutants, the MD-derived values of the torsional modulus lie within these distributions which give the statistical uncertainties of the $\kappa$ estimation from four independent 100-ns trajectories. Because both BD-derived distributions of $\kappa$ are relatively narrow and centered on the equilibrium values, we concluded that our MD reliably captures the elastic properties of $F_1$ at the atomistic level.

**Minimal Model of the $F_1$ Elasticity.** This model (Fig. 5) serves to describe, in a quantitative manner, the spatial heterogeneity of the elastic properties of the $F_1$-ATPase using the minimal number of rotary degrees of freedom. In our treatment, the $F_1$ motor is represented as a set of $N$ harmonically coupled concentric segments, oriented perpendicularly to the threefold pseudosymmetry axis of the $\alpha_3\beta_3$-subunit. The harmonic coupling constants $\{\kappa_{ij}\}$, where $i$ and $j$ denote the respective segments, quantify the strength of torsional interactions between the segments and, thereby, reflect the rotational correlations between them. The partition into segments and the coupling constant values were optimized, in a systematic approach, to best reproduce the distribution of angular fluctuations observed from the atomistic MD simulations. Additionally, a local description was assumed in which only the segments that are in close contact to each other in the $F_1$ structure are directly coupled to each other via a coupling constant $\kappa_{ij}$; all other coupling constants are set to zero. In particular, each segment of the $\alpha_3\beta_3$-penetrating portion of γ is coupled to a single opposite segment of the stator.

Angular deviation of the $i$th segment with respect to the equilibrium (average) position is denoted as $\theta_i$. The elastic energy stored in the protein structure due to the set of torsional deformations $\boldsymbol{\theta} = \{\theta_1,\ldots,\theta_N\}$ is $V = \frac{1}{2}\boldsymbol{\theta}^T\mathbf{K}\boldsymbol{\theta}$, where $\mathbf{K}$ is a quasiharmonic Hessian whose entries depend on the "network" of couplings between the segments. In this quasiharmonic approximation, the equilibrium probability distribution of $\boldsymbol{\theta}$ is thus given by a multivariate normal distribution (1), $p(\boldsymbol{\theta}) \propto \exp(-\frac{1}{2}\boldsymbol{\theta}^T\mathbf{K}\boldsymbol{\theta}/k_BT) \propto \exp(-\frac{1}{2}\boldsymbol{\theta}^T\mathbf{C}^{-1}\boldsymbol{\theta})$, where $\mathbf{C}$ is a covariance matrix of angular fluctuations $\langle\boldsymbol{\theta}\boldsymbol{\theta}^T\rangle$, with $k_BT\mathbf{C}^{-1} = \mathbf{K}$.

To determine the model parameters, the $\mathbf{C}$ was first computed as the average over our MD trajectories for different possible partitions of $F_1$ into segments. To obtain these partitions in a systematic way, the rotor and stator were initially dissected into approximately 0.5-nm segments oriented perpendicularly to the $\alpha_3\beta_3$-symmetry axis. Only the innermost layer of the $\alpha_3\beta_3$ located within 0.7 nm of the γ-subunit and thus interacting directly with the rotor was divided into separate segments, paralleling the rotor division to satisfy the locality assumption. The rest of the stator was modeled as two segments: one, labeled 8 in Fig. 5, encompassing the torsionally stiff central domains of the α- and β-chains, and the other, labeled 9, representing the immobile β-barrels, with respect to which the angular fluctuations were calculated. The highly flexible and weakly interacting single-helix tip of γ for which it was difficult to obtained well-defined angular fluctuations was not included in the analysis. By systematically joining together the increasing number of adjacent 0.5-nm segments, a set of different partitions was obtained. The $\alpha_3\beta_3$-penetrating and the protruding portions of the rotor, as the two dynamically independent entities (see *Central Shaft Elasticity: Heterogeneity of Torsional Modulus* in the main text), were treated separately when joining the 0.5-nm building blocks.

By equating the respective entries of the computed $k_BT\mathbf{C}^{-1}$ with nonzero entries of the assumed form of the corresponding $\mathbf{K}$, a set of overdetermined systems of linear equations was obtained. These systems were then solved for the individual quasiharmonic coupling constants $\{\kappa_{ij}\}$, using the standard least squares method. The model with the smallest value of the average over the estimated standard errors of the solution $\{\kappa_{ij}\}$ was selected as the optimal one and is presented schematically in Fig. 5. The optimized coupling constants $\{\kappa_{ij}\}$ for this model and the corresponding estimated standard errors from the least square solution are shown in Table S2.

The resulting harmonic model contains two 2.0-nm-thick segments, labeled 4 and 5 in Fig. 5, in the $\alpha_3\beta_3$-penetrating part of the rotor and three segments, the 1.5-nm-thick segments 2 and 3, and the 1.0-nm-thick segment 1, in the protruding part of the rotor. To compare, however, the strength of the coupling to the individual stator subunits in the strongly interacting helix–turn–helix (HTH) region, we additionally constructed a model in which segment 4 was coupled to six separate subsegments of segment 6, representing HTH motifs of all six stator subunits. For this partition, we obtained the constants of $320 \pm 181$, $240 \pm 107$, $200 \pm 129$, and $100 \pm 82$ pNnm describing the coupling of segment 4 with subunits $\beta_{DP}$, $\beta_{TP}$, $\alpha_E$, and $\beta_E$, respectively. Virtually no coupling to the γ-subunit was found for the $\alpha_{DP}$ and $\alpha_{TP}$ subunits. The obtained coupling strengths are consistent with the results of the rotor-stator interaction analysis presented in *Structural Determinants of the Coupling Between Rotor and Stator* in the main text. These coupling values should, however,

be treated with caution because the obtained uncertainties are large and the overall coupling strength between segment 4 and segment 6 in this model is almost two times larger than $\kappa_{46}$ in the optimal model, suggesting a breakdown of the local harmonic approximation.

For the optimal model, derived as described (Fig. 5), the equilibrium probability distribution of angular fluctuations is given by

$$p(\boldsymbol{\theta}) = \frac{1}{(2\pi k_{\mathrm{B}}T)^4 \det(\mathbf{K}^{-1})} \exp(-\boldsymbol{\theta}^T \mathbf{K} \boldsymbol{\theta} / 2k_{\mathrm{B}}T),$$

where the Hessian matrix $\mathbf{K}$ is as follows:

$$\begin{pmatrix}
\kappa_{12} & -\kappa_{12} & 0 & 0 & 0 & 0 & 0 & 0 \\
-\kappa_{12} & \kappa_{12}+\kappa_{23} & -\kappa_{23} & 0 & 0 & 0 & 0 & 0 \\
0 & -\kappa_{23} & -\kappa_{34} & 0 & 0 & 0 & 0 & 0 \\
0 & 0 & -\kappa_{34} & \kappa_{34}+\kappa_{45}+\kappa_{46} & -\kappa_{45} & -\kappa_{46} & 0 & 0 \\
0 & 0 & 0 & -\kappa_{45} & \kappa_{45}+\kappa_{57} & 0 & -\kappa_{57} & 0 \\
0 & 0 & 0 & -\kappa_{46} & 0 & \kappa_{46}+\kappa_{67}+\kappa_{68} & -\kappa_{67} & -\kappa_{68} \\
0 & 0 & 0 & 0 & -\kappa_{57} & -\kappa_{67} & \kappa_{57}+\kappa_{67}+\kappa_{78} & -\kappa_{78} \\
0 & 0 & 0 & 0 & 0 & -\kappa_{68} & -\kappa_{78} & \kappa_{68}+\kappa_{78}+\kappa_{89}
\end{pmatrix}.$$

The obtained set of harmonically coupled segments approximates the shape of the free energy surface $G(\boldsymbol{\theta}) = -k_{\mathrm{B}}T \ln p(\boldsymbol{\theta})$ along the rotary degrees of freedom in the vicinity of the rotor resting position observed in the vast majority of the crystal structures. By integrating the joint probability distribution $p(\boldsymbol{\theta}) \propto \exp(-G(\boldsymbol{\theta})/k_{\mathrm{B}}T)$ over all angles except $\theta_i$, one obtains the Gaussian marginal probability distribution $p(\theta_i)$ and the corresponding one-dimensional free energy curve $G(\theta_i) = -k_{\mathrm{B}}T \ln p(\theta_i)$ governing the overall angular fluctuation of the $i$th segment. Taking the second derivative of $G(\theta_i)$ with respect to $\theta_i$, we obtain the relation between the curvature of this function, i.e., the overall torsional modulus $\kappa_i$, and the individual coupling constants $\{\kappa_{ij}\}$ quantifying the torsional interactions between the segments. For example, if $\kappa_{89} \to \infty$ is assumed, for segment 4 we obtain

$$\kappa_4 = \frac{\kappa_{46}\kappa_{57}[\kappa_{68}\kappa_{78} + \kappa_{67}(\kappa_{68}+\kappa_{78})] + \kappa_{45}\{\kappa_{57}[\kappa_{67}\kappa_{68} + (\kappa_{67}+\kappa_{68})\kappa_{78}] + \kappa_{46}[(\kappa_{57}+\kappa_{67})\kappa_{68} + (\kappa_{57}+\kappa_{67}+\kappa_{68})\kappa_{78}]\}}{\kappa_{57}[\kappa_{67}(\kappa_{46}+\kappa_{68}) + (\kappa_{46}+\kappa_{67}+\kappa_{68})\kappa_{78}] + \kappa_{45}[\kappa_{67}(\kappa_{57}+\kappa_{78}) + \kappa_{46}(\kappa_{57}+\kappa_{67}+\kappa_{78}) + \kappa_{68}(\kappa_{57}+\kappa_{67}+\kappa_{78})]}.$$

Such relations were used to decompose the overall torsional moduli, as measured in experiment or observed in the simulation, into contributions arising from relevant structural elements and intermolecular couplings.

1. Grubmüller H (1995) Predicting slow structural transitions in macromolecular systems: Conformational flooding. *Phys Rev E* 52:2893–2906.

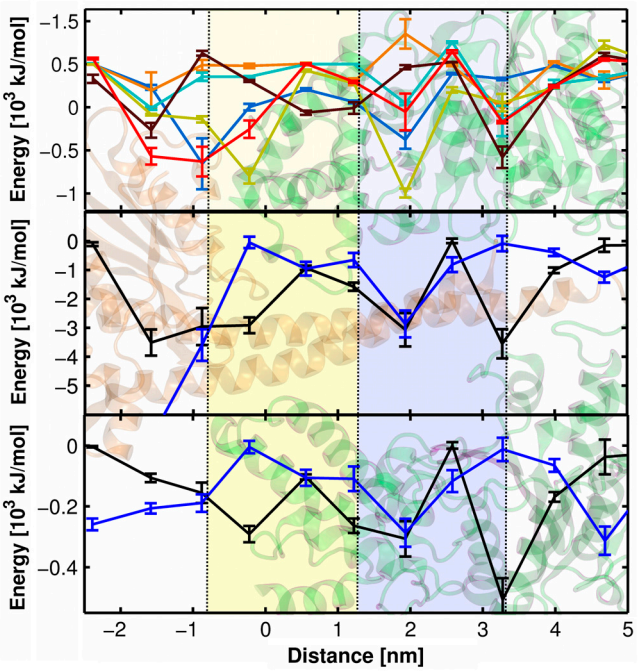


**Fig. S1.** Interaction energies between the rotor and the stator of the $F_1$ motor as a function of the position along the global axis. The position was measured as the distance of the segment center of mass from the average position of the β-DELSEED motifs with the positive sign toward the top of the structure and with the negative sign in the opposite direction. (*Top*) Contributions to the total interaction energy from individual stator chains. (*Middle*) Total interaction energy of the rotor with the stator (black) and with the water solution (blue). (*Bottom*) Total interaction energy of the rotor with the stator (black) and with the solvent (blue), normalized by the number of rotor residues that are exposed to the environment. The highlighted areas 4 and 5 show the position of the respective rotor segments in the minimal harmonic model of $F_1$ torsional elasticity presented in Fig. 5. The error bars represent the standard errors determined using a block averaging technique.

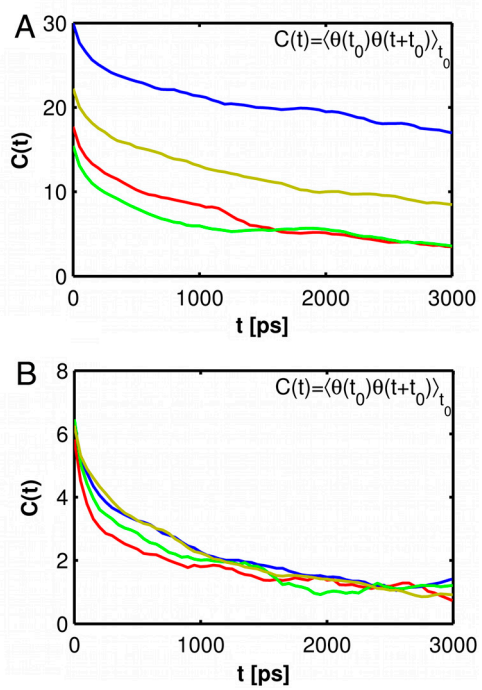


**Fig. S2.** Autocorrelation functions for the angle of rotation of the segment around the global axis calculated for the CL1- (*A*) and CL2-cross-linked (*B*) $F_1$ motor. $\langle\rangle_{t_0}$ denotes averaging over initial times $t_0$; note that average $\langle\theta\rangle_{t_0} = 0$.

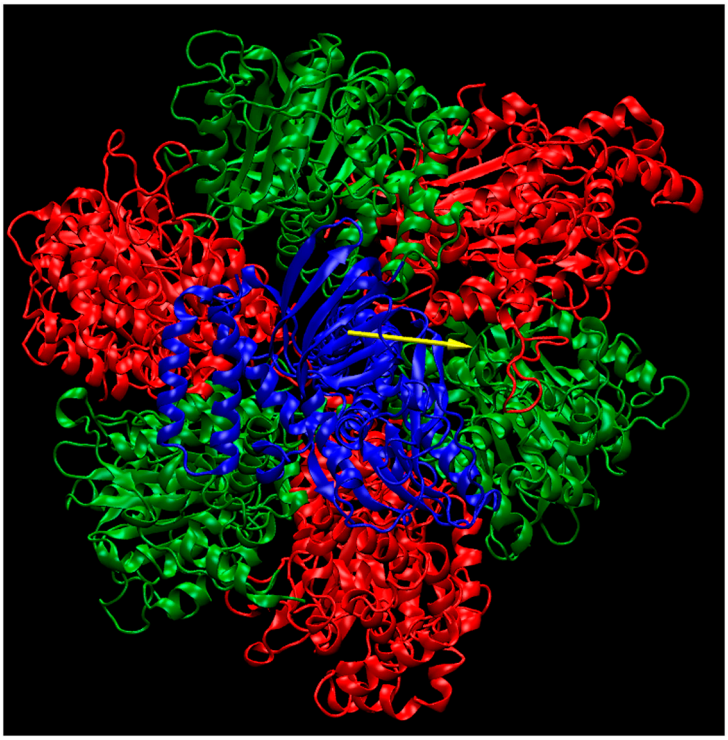

**Movie S1.** Angular fluctuations of the $F_1$-ATPase central shaft, as viewed from the membrane.

Movie S1 (MPG)

**Table S1. Frequency of hydrogen bonds formation between different residues of the rotor and stator***

| Rotor (γ) res. | Stator chain | Stator res. | Frequency† |
|---|---|---|---|
| **Upper bearing** | | | |
| Glu-261 | $\beta_{DP}$ | Val-279 (bb) | 0.61 |
| Arg-252 | $\alpha_{TP}$ | Asp-333 | 0.59 |
| Leu-272 | $\alpha_{DP}$ | Arg-286 | 0.37 |
| Thr-259 | $\beta_{E}$ | Val-279 (bb) | 0.31 |
| Ala-1 (bb) | $\alpha_{DP}$ | Asp-333 | 0.22 |
| Lys-260 | $\alpha_{DP}$ | Glu-292 | 0.21 |
| **Lower bearing** | | | |
| Arg-254 | $\beta_{E}$ | Asp-319 | 0.63 |
| Gln-255 | $\beta_{E}$ | Thr-318 | 0.58 |
| Arg-254 | $\beta_{E}$ | Asp-316 | 0.30 |
| Lys-4 | $\beta_{DP}$ | Asp-316 | 0.30 |
| Asn-251 | $\beta_{E}$ | Asp-316 | 0.29 |
| **C-terminal stator domains** | | | |
| Leu-77 (bb) | $\beta_{TP}$ | Glu-395 | 0.97 |
| Arg-133 | $\beta_{DP}$ | Asp-394 | 0.96 |
| Arg-75 | $\beta_{DP}$ | Glu-395 | 0.96 |
| Arg-75 | $\beta_{DP}$ | Asp-394 | 0.87 |
| Gly-79 (bb) | $\beta_{TP}$ | Glu-395 | 0.85 |
| Arg-8 | $\beta_{DP}$ | Asp-386 | 0.84 |
| Cys-78 (bb) | $\beta_{TP}$ | Glu-395 | 0.69 |
| Arg-33 | $\alpha_{E}$ | Asp-411 | 0.45 |
| Arg-9 | $\beta_{TP}$ | Asp-386 | 0.42 |
| Arg-118 | $\beta_{TP}$ | Glu-399 | 0.42 |
| Lys-30 | $\alpha_{E}$ | Asp-409 | 0.39 |
| Arg-36 | $\beta_{E}$ | Glu-395 | 0.37 |
| Tyr-31 | $\beta_{E}$ | Glu-395 | 0.33 |
| Lys-24 | $\beta_{E}$ | Asp-386 | 0.30 |
| Ser-114 | $\beta_{TP}$ | Glu-398 | 0.27 |
| Asn-15 | $\alpha_{E}$ | Ala-402 (bb) | 0.24 |
| Lys-111 | $\beta_{TP}$ | Glu-395 | 0.23 |
| Lys-18 | $\alpha_{E}$ | Glu-399 | 0.20 |

*Only residue pairs with frequency of hydrogen bond above 0.2 are shown. All bonds are formed via side-chain groups unless explicitly marked with (bb), in which case the backbone peptide group participates in bond formation. As geometrical criterion for the presence of a hydrogen bond we used D—A distance < 0.35 nm and D–A–H angle <30°, where D, A, and H are donor, acceptor, and hydrogen, respectively.

†Calculated as the fraction of MD frames for which the bond was present.

**Table S2. Summary of the $F_1$ torsional elasticity model**

| | | | Twist angle* (°) | | Stored energy† (kcal/mol) | |
|---|---|---|---|---|---|---|
| Elastic constant | Value (pNnm) | Error | Rigid | Flexible | rigid | flexible |
| $\kappa_{12}$ | 950 | ± 24 | 8.87 | 2.15 | 3.26 (29.5%) | 0.190 (7.1%) |
| $\kappa_{23}$ | 2,760 | ± 26 | 3.05 | 0.74 | 1.12 (10.2%) | 0.066 (2.5%) |
| $\kappa_{34}$ | 2,040 | ± 31 | 4.13 | 1.00 | 1.52 (13.7%) | 0.090 (3.4%) |
| $\kappa_{45}$ | 1,000 | ± 51 | 4.30 | 1.04 | 0.81 (7.3%) | 0.048 (1.8%) |
| $\kappa_{46}$ | 550 | ± 56 | 7.49 | 1.82 | 1.35 (12.2%) | 0.079 (2.9%) |
| $\kappa_{57}$ | 350 | ± 72 | 8.94 | 2.17 | 1.22 (11.1%) | 0.072 (2.7%) |
| $\kappa_{68}$ | 820 | ± 116 | 6.45 | 1.57 | 1.49 (13.5%) | 0.088 (3.3%) |
| $\kappa_{67}$ | 370 | ± 56 | 3.18 | 1.40 | 0.16 (1.5%) | 0.032 (1.2%) |
| $\kappa_{78}$ | 4,450 | ± 116 | 0.70 | 0.17 | 0.1 (0.9%) | 0.005 (0.2%) |
| $\kappa_{89}$ | >10,000 | | ~ | ~ | ~ | ~ |
| $\kappa_{int}$ | 90 | | — | 22.6 | — | 2.01 (75.0%) |

*Caused by 30° rotation corresponding to the rotation of the 12-subunits *c* ring by a single-proton step. Two values are presented depending on whether the interface with $F_o$ is torsionally "flexible" with the torsional stiffness $\kappa_{int} = 90$ pNnm (see text) or completely "rigid" with $\kappa_{int} = \infty$

†Corresponding to Twist angle. In the brackets the percentage of the total elastic energy stored in the structure is shown.